

Seismological structure of the upper mantle: a regional comparison of seismic layering

James B. Gaherty^{*}, Mamoru Kato¹, Thomas H. Jordan

Department of Earth, Atmospheric, and Planetary Sciences, Massachusetts Institute of Technology, Cambridge, MA 02139, USA

Received 8 May 1997; revised 8 March 1998; accepted 3 September 1998

Abstract

We investigate seismic layering (i.e., discontinuities, regions of anomalous velocity gradients, and anisotropy) and its lateral variability in the upper mantle by comparing seismic models from three tectonic regions: old (~ 100 Ma) Pacific plate, younger (~ 40 Ma) Philippine Sea plate, and Precambrian western Australia. These models were constructed by combining two data sets: ScS-reflectivity profiles, which provide travel times and impedance contrasts across mantle discontinuities, and observations of frequency-dependent travel times of three-component turning (S, sS, SS, sSS, SSS, Sa) and surface (R_1 , G_1) waves, which constrain the anisotropic velocity structure between discontinuities. The models provide a better fit to observed seismograms from these regions than the current generation of global tomographic models. The Australian model is characterized by high shear velocities throughout the upper 350 km of the mantle, with no low-velocity zone (LVZ) in the isotropically averaged shear velocities. In contrast, the oceanic models are characterized by a thin, high-velocity seismic lid underlain by a distinct LVZ, with a sharp boundary (the G discontinuity) separating them. The G is significantly deeper beneath the western Philippine Sea plate than beneath the (older) Pacific (89 and 68 km, respectively), implying that thermal cooling alone does not control the thickness of the lid. We interpret this discontinuity as a compositional boundary marking the fossilized base of the melt separation zone (MSZ) active during sea-floor spreading. No discontinuity is detected at the base of the LVZ in the oceanic models. The S velocity gradient between 200 and 410 km depth is much steeper in the oceans than beneath Australia. This high oceanic gradient is probably controlled by a decrease in the homologous temperature over this depth interval. The relative depths of the transition zone (TZ) discontinuities are consistent with Clapeyron slopes expected for an olivine-dominated mineralogy. The 660-km discontinuity displays variability in its amplitude that appears to correlate with its depth; shallow and bright beneath the Pacific, deep and dim beneath Australia and the Philippine Sea. Such behavior is possibly caused by the juxtaposition of the olivine and garnet components of the phase transition. Radial anisotropy extends through the upper 250 km of the mantle in the Australia model and through the upper 160 km of the two oceanic models. The magnitude of anisotropy is consistent with that expected for models of horizontally oriented olivine, and the localization of anisotropy in the shallowest upper mantle implies that it reflects strain associated with past or present tectonic events. © 1999 Elsevier Science B.V. All rights reserved.

Keywords: Seismic structure; Upper mantle; Discontinuities; Anisotropy

^{*} Corresponding author. School of Earth and Atmospheric Sciences, Georgia Institute of Technology, Atlanta, GA 30332, USA. Fax: +1-404-894-5638; E-mail: gaherty@eas.gatech.edu

¹ Present address: Department of Geophysics, Kyoto University, Kyoto, Japan.

1. Introduction

We have studied the seismic stratification of the Earth's upper mantle by inverting a novel and powerful combination of travel time data from corridors traversing the Australian continent, the central Pacific Ocean, and the Philippine Sea (Fig. 1). On this scale, some of the major differences in path averaged shear velocities can be resolved by global tomographic models. For example, model S12_WM13 of Su et al. (1994) shows that Australia has higher shear velocities than the oceanic paths in the upper 400 km

and that the central Pacific Ocean has a faster lid than the Philippine Sea (Fig. 2). These contrasts reflect the lateral temperature and/or compositional differences in the upper mantle that we seek to understand. However, the picture of the upper mantle obtained from S12_WM13 and many other published global tomographic models is necessarily incomplete, because most were derived by holding the anisotropy and discontinuity structure constant during the inversion.

The purpose of our study is to investigate regional variations in the depths of upper mantle discontinu-

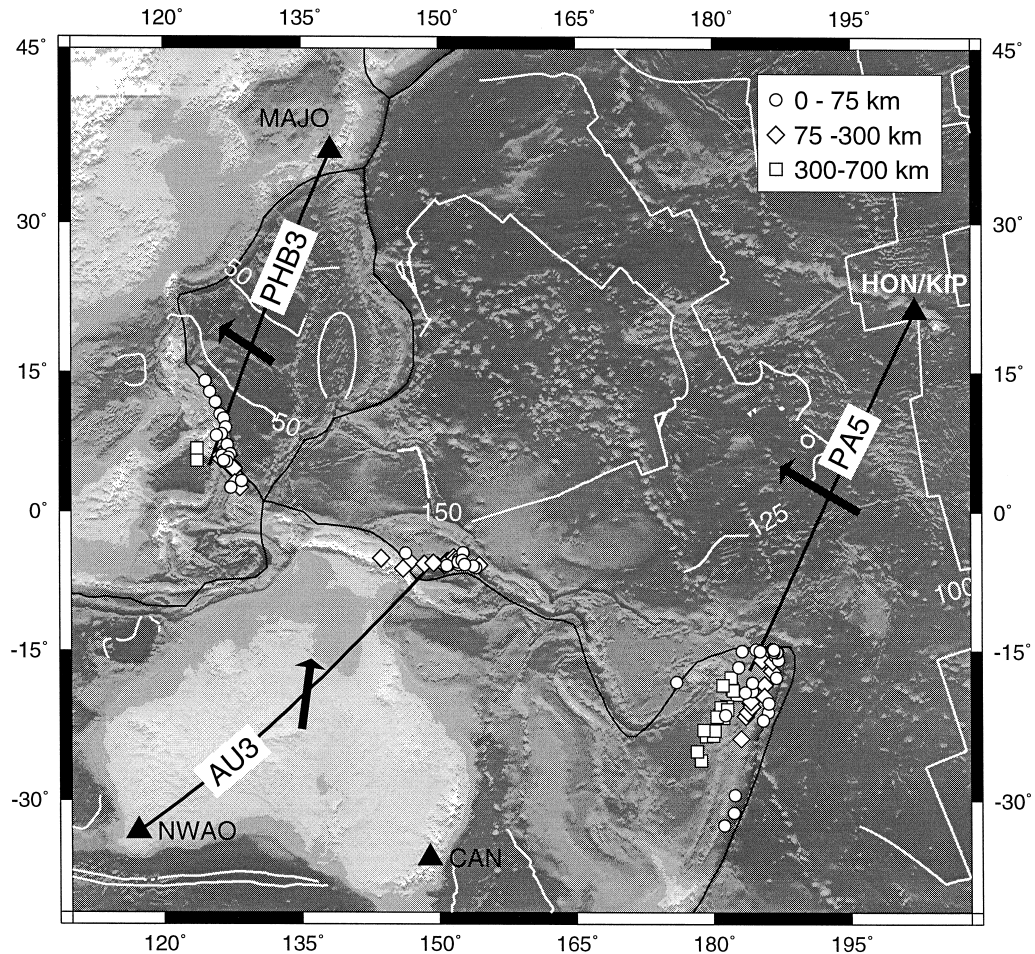


Fig. 1. Seismic corridors (solid black lines) modeled in this study; each corridor represents the average path connecting a source array (open circles, squares, and diamonds) with a broad-band seismic station (triangles). We model three corridors, one traversing Australia from New Britain earthquakes to NWA0 (labeled AU3), one traversing the central Pacific from Tonga/Fiji events to HON/KIP (labeled PA5), and one crossing the Philippine Sea basin from the Philippine events to MAJO (labeled PHB3). Ocean plate magnetic isochrons of Mueller et al. (1993) are plotted in white. Also plotted are arrows which represent the NUVEL-1 plate motions relative to a hotspot reference frame (Gripp and Gordon, 1990).

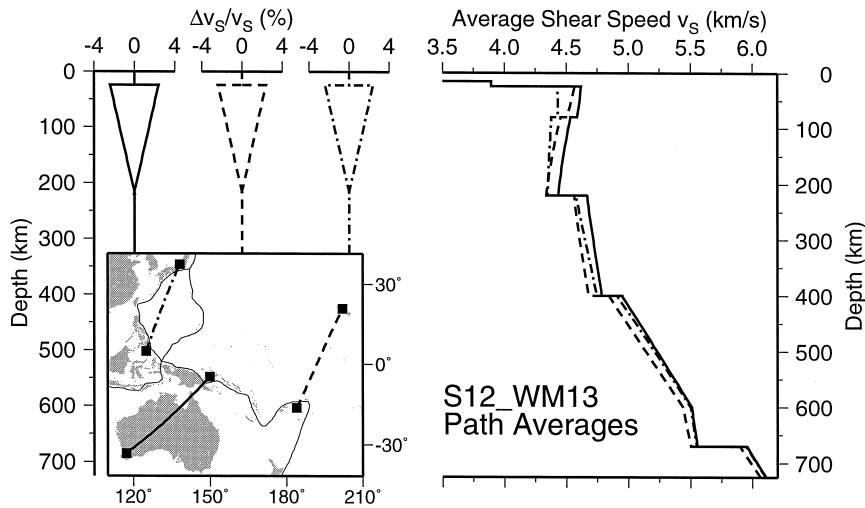


Fig. 2. Shear wave structures obtained from the global tomographic model S12_WM13 of Su et al. (1994) for the seismic corridors corresponding to the AU3 (solid line), PA5 (dashed line), and PHB3 (dash-dotted line) regional models. These path averages were calculated by integrating the isotropic shear velocity perturbations in S12_WM13 (described laterally by spherical harmonics to angular order 12, and vertically by Chebyshev polynomials to order 13) along each source–receiver path shown on the inset map, and applying these path average perturbations to both shear velocities (v_{SH} and v_{SV}) in PREM. For each path average, the mean shear speed ($\bar{v}_S = (v_{SH} + v_{SV})/2$) is plotted in the right panel, and the anisotropic deviations from this mean ($(v_{SV} - \bar{v}_S)/\bar{v}_S$ and $(v_{SH} - \bar{v}_S)/\bar{v}_S$, in percent) are plotted in the left panels. The negative anisotropic deviations are associated with v_{SV} , the positive with v_{SH} .

ities and the changes in material properties across them, including anisotropy, and to relate these variations to geodynamics and the development of the plate–tectonic boundary layers. Previous work has demonstrated that these variations can be seismologically significant. Lateral differences have been observed in the depth and reflectivity of the 410- and 660-km discontinuities (e.g., Revenaugh and Jordan, 1991a; Vidale and Benz, 1992; Shearer, 1993), the character of shallow upper mantle reflectors (e.g., Revenaugh and Jordan, 1991b; Vidale and Benz, 1992; Shearer, 1993; Zhang and Lay, 1993), and the orientation of shear wave anisotropy (Vinnik et al., 1992; Silver, 1996). Incorporating these observations into seismological models is difficult, however, because the sampling of the upper mantle afforded in such studies is usually more localized than that obtained using conventional surface wave and body wave methods. Moreover, the standard methods often use different representations of the seismogram to analyze different waveforms; SH waveforms are usually represented as a summation over rays (e.g., Grand and Helmberger, 1984a,b), while PSV waveforms are modeled as a summation over traveling

modes (e.g., Nolet, 1975; Lerner-Lam and Jordan, 1983, 1987). The mutual consistency of the data sets is thus compromised by differing wave-theoretic approximations, especially with regard to the waveform splitting effects that are diagnostic of upper mantle anisotropy.

2. Methodology

2.1. Data analysis

A key aspect of this study is the unified methodology employed to measure and invert the data for all three corridors. The corridors were defined by the wave paths between localized source arrays and three-component, high-performance seismic stations, chosen to traverse relatively homogeneous tectonic regions. To obtain the best sampling of the upper mantle, we selected source arrays in deep seismic zones with a full range of focal depths, at epicentral distances of between 25 and 55° from the chosen receivers. The first step in the data analysis, taken by Revenaugh and Jordan (1991a,b,c), was to stack the

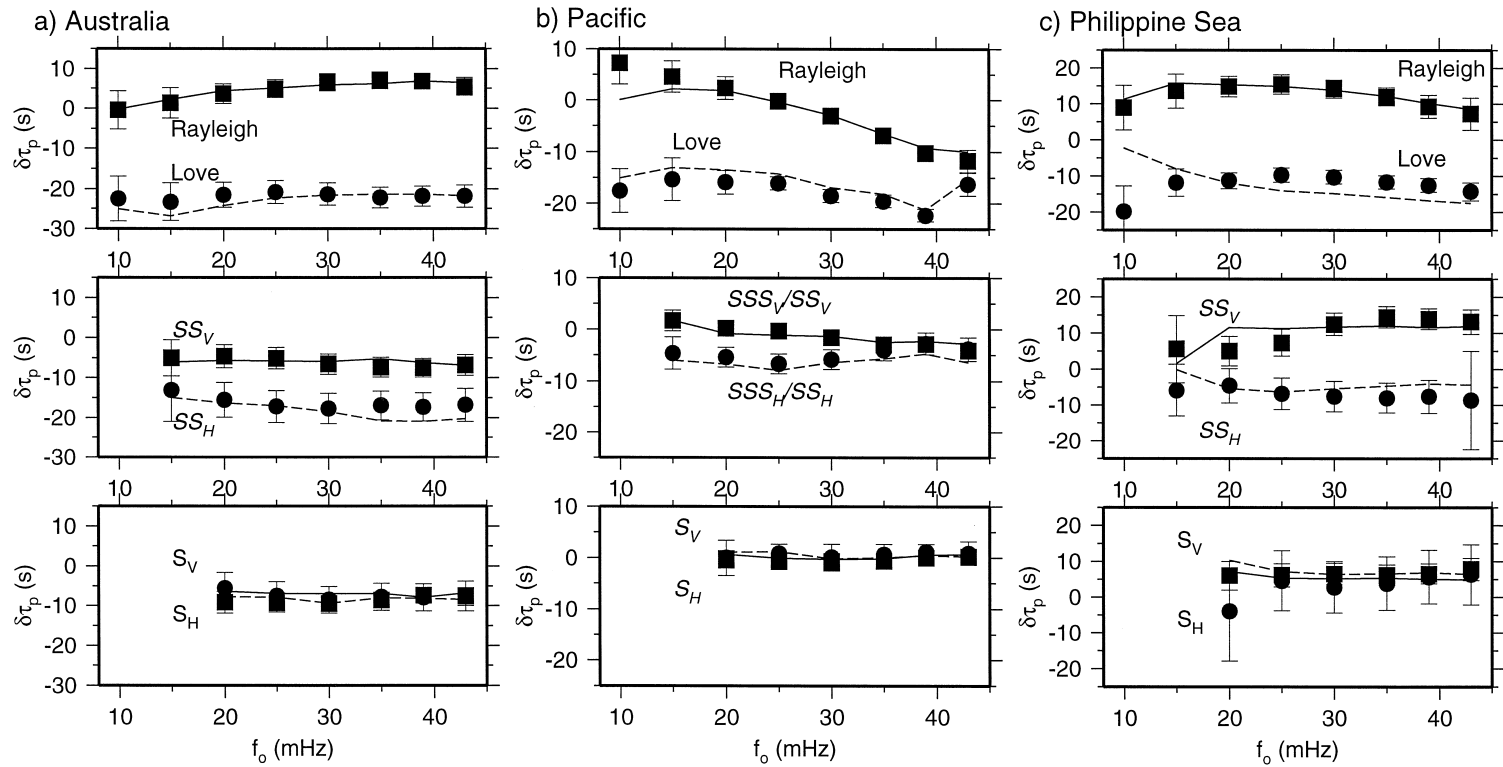


Fig. 3. Summary of the frequency-dependent travel time data. Average phase delays $\delta\tau_p$ for (a) the Australia corridor, (b) the Pacific corridor, and (c) the Philippine Sea corridor, referenced to corridor-specific isotropic starting models and plotted against frequency for surface waves (*top panels*), SS and SSS waves (*middle*), and S waves (*bottom*). Points with standard errors are averages of measurements for each seismic phase from vertical (*squares*) and transverse (*circles*) seismograms, summarizing the frequency-dependent travel times used in the inversions; solid and dashed lines are corresponding averages computed for the models of Fig. 4. The total number of phase delay measurements summarized are: Australia, 797; Pacific, 1499; Philippine Sea, 1039.

ScS reverberations from a subset of these seismograms for the shear wave reflectivity profile of the mantle within each seismic corridor. This procedure first involved fitting the waveforms of the primary ScS_n and sScS_n phases (zeroth-order reverberations) to determine the whole-mantle ScS travel time and attenuation factor (Q_{ScS}) for each path. With this calibration, the travel times and amplitudes of the primary reflections from upper mantle discontinuities (first-order reverberations) were determined via a stacking and migration procedure. The resulting corridor-specific profiles of mantle reflectivity provided the vertical travel times to, and SV impedance contrasts across, all mantle discontinuities. This procedure was able to detect, measure, and locate impedance variations as small as 1%, and the vertical travel times and impedance contrasts provide precise, layered frameworks for the regional upper mantle structures. We follow the conventions of Revenaugh and Jordan (1991b) in designating internal discontinuities above 400 km by a capital letter (M = Mohorovicic, H = Hales, G = Gutenberg, L = Lehmann) and TZ discontinuities by their nominal depths in kilometers; e.g., 410, 520, 660, 710 and 900.

The second step was to measure an extensive set of frequency-dependent travel times from surface waves, body waves, and guided waves of all polarizations (Fig. 3). The analyzed seismic phases included S, sS, SS, sSS, SSS, Sa, R_1 , and G_1 , and the travel times were measured by cross-correlating observed seismograms with spherical Earth synthetic seismograms computed by mode summation (Gee and Jordan, 1992). At the epicentral distances and frequencies (10–45 mHz) used here, these phases are affected by complex interference of multiple refractions, reflections, and conversions from upper mantle discontinuities, and they show clear evidence of splitting between SH and P–SV components, indicative of anisotropy (Fig. 3). Fréchet kernels used to invert these data accounted for radial anisotropy, frequency-dependent diffractions, and other wave-propagation effects, including the interference from other seismic phases (Gee and Jordan, 1992; Gaherty et al., 1996). The number of measured travel times ranged from approximately 800 from the Australian corridor to nearly 1500 from the Pacific corridor. Such data provide good constraints on the radially

anisotropic velocities and gradients (especially the shear velocities) between the discontinuities.

2.2. Inversion

The two data sets from each corridor were jointly inverted for regional radially anisotropic (transversely isotropic) models of the upper mantle, defined by six medium parameters (e.g., Dziewonski and Anderson, 1981): mass density, $\rho(z)$; the speeds of horizontally and vertically propagating P waves, $v_{\text{PH}}(z)$ and $v_{\text{PV}}(z)$; the speed of horizontally propagating, transversely polarized shear waves, $v_{\text{SH}}(z)$; the speed of a shear wave propagating either horizontally with a vertical polarization or vertically with horizontal polarization (e.g., ScS reverberations), $v_{\text{SV}}(z)$; and a parameter that governs the variation of the wave speeds at oblique propagation angles, $\eta(z)$. The models are frequency dependent, with the attenuation structure along each corridor chosen to satisfy the observed Q_{ScS} in conjunction with surface wave amplitude data. Our modeling procedures sought minimal structure: first-order discontinuities were suppressed unless detected by ScS reverberations; linear gradients were maintained between discontinuities; second-order discontinuities (i.e., changes in gradient between two observed first-order discontinuities) were only allowed if a single layer was unable to satisfy the data; and isotropy ($v_{\text{PH}} = v_{\text{PV}}$, $v_{\text{SH}} = v_{\text{SV}}$, $\eta = 1$) was required wherever consistent with the data. Various inversion experiments were performed to test for the depth distribution of the anisotropy. The non-linear analysis procedure was fully iterated at least twice for each corridor, with each iteration including complete remeasurement of the data using synthetic seismograms computed from the new model and recalculation of their associated partial derivatives.

The data sets were complementary, in that the ScS reverberation data provided strong constraints on the discontinuity depths and SV impedance contrasts, while the extensive shear wave travel time data were most sensitive to the shear velocities between discontinuities. Using the formal posterior uncertainties as a guide, we conservatively assess our standard errors of estimation to be of order 3–5 km for the depths of the major discontinuities (M, G, 410, 660), 5–10 km for the smaller discontinuities

(H, L), approximately ± 0.05 km/s in the layer averages of v_{SH} and v_{SV} , and $\sim 1\%$ in shear anisotropy through the upper mantle and TZ. Our shear wave data are relatively insensitive to the compressional velocities and density, however, and we constrained these parameters by incorporating a complementary set of mineral physics data. At six discrete depths between 250 and 780 km, we required the density ρ and bulk sound velocity $v_\phi = (v_P^2 - 4v_S^2/3)^{1/2}$ to satisfy the estimates obtained by Ita and Stixrude (1992) for a pyrolite mineralogy, assigning a standard error of $\pm 1\%$ to each estimate. These parameters can be inferred with reasonable precision from laboratory observations; moreover, the choice of a pyrolite composition is not particularly restrictive, since similar estimates for competing mineralogical models (e.g., high-aluminum piclogite) differ from pyrolite by less than the assigned errors (Ita and Stixrude, 1992). These constraints had little effect on the estimated shear velocities, but they ensured that the relative behavior of the density, shear, and compressional profiles conform to realistic mineralogies.

We have completed the modeling for the three corridors in Fig. 1, and the final models are presented in Tables 1–3. A complete discussion of the analysis and inversion is presented by Gaherty et al. (1996) for the Pacific corridor, with details associated with Australia and the Philippine Sea provided

by Gaherty and Jordan (1995) and Kato and Jordan (1998), respectively. Here we investigate the regional variation of mantle layering as described by these three models. Because the shear velocities are the best resolved parameters in our model, they are the focus of our discussion.

Fig. 4 displays the S wave structures from our models, designated AU3, PA5, and PHB3 for the Australia, Pacific, and Philippine Sea corridors, respectively. Comparing Figs. 2 and 4, it appears that the regional models capture a number of the important features of upper mantle structure that cannot be discerned in S12_WM13. These features include substantial heterogeneity in lid and low-velocity zone (LVZ) structure in the uppermost mantle, and large variations in the discontinuity depths and amplitudes, in the maximum depth of the anisotropy, and in the shear-speed gradients, especially between 100 and 400 km. Moreover, S12_WM13 has a large jump in v_S across a Lehmann (L) discontinuity at 220 km (inherited from its reference model, PREM), while the isotropic shear speeds at this depth are essentially continuous in our models.

A simple visual evaluation indicates that our models better characterize upper mantle structure in these regions. Fig. 5 displays representative seismograms for the three corridors, and it compares these observations with synthetics calculated for the path averaged models in Tables 1–3 as well as global model

Table 1
Model AU3*

z (km)	ρ (Mg/m ³)	v_{SV} (km/s)	v_{SH} (km/s)	v_{PV} (km/s)	v_{PH} (km/s)	η	Q_μ
0.0	2.85	3.62	3.62	6.05	6.05	1.00	300
30.0	2.85	3.62	3.62	6.05	6.05	1.00	300
30.0	3.30	4.28	4.40	8.00	8.15	0.90	300
54.0	3.30	4.28	4.40	8.00	8.15	0.90	300
54.0	3.40	4.56	4.68	8.23	8.52	0.90	300
252.0	3.44	4.52	4.70	8.28	8.61	0.90	300
252.0	3.45	4.63	4.63	8.45	8.45	1.00	120
406.0	3.58	4.80	4.80	8.88	8.88	1.00	120
406.0	3.69	5.07	5.07	9.31	9.31	1.00	312
499.0	3.85	5.19	5.19	9.64	9.64	1.00	312
499.0	3.88	5.23	5.23	9.67	9.67	1.00	312
659.0	4.00	5.58	5.58	10.21	10.21	1.00	312
659.0	4.21	5.94	5.94	10.72	10.72	1.00	312
861.0	4.50	6.28	6.28	11.21	11.21	1.00	312

Table 2
Model PA5*

z (km)	ρ (Mg/m ³)	v_{SV} (km/s)	v_{SH} (km/s)	v_{PV} (km/s)	v_{PH} (km/s)	η	Q_μ
0.0	1.03	0.00	0.00	1.50	1.50	1.00	9999
5.0	1.03	0.00	0.00	1.50	1.50	1.00	9999
5.0	1.50	0.92	0.92	2.01	2.01	1.00	9999
5.2	1.50	0.92	0.92	2.01	2.01	1.00	9999
5.2	3.03	3.68	3.68	5.93	5.93	1.00	150
12.0	3.03	3.68	3.68	5.93	5.93	1.00	150
12.0	3.34	4.65	4.84	8.04	8.27	0.90	150
68.0	3.38	4.67	4.83	8.06	8.30	0.90	150
68.0	3.35	4.37	4.56	7.88	8.05	0.90	50
166.0	3.41	4.26	4.34	8.04	8.09	1.00	50
166.0	3.42	4.29	4.29	8.06	8.06	1.00	150
415.0	3.58	4.84	4.84	8.92	8.93	1.00	150
415.0	3.71	5.04	5.04	9.29	9.29	1.00	150
507.0	3.85	5.20	5.20	9.64	9.64	1.00	150
507.0	3.88	5.28	5.28	9.71	9.71	1.00	150
651.0	4.02	5.43	5.43	10.11	10.11	1.00	150
651.0	4.29	5.97	5.97	10.76	10.76	1.00	231
791.0	4.46	6.23	6.23	11.08	11.08	1.00	231
791.0	4.46	6.23	6.23	11.08	11.08	1.00	231
801.0	4.46	6.24	6.24	11.10	11.10	1.00	231

Table 3
Model PHB3^a

z (km)	ρ (Mg/m ³)	v_{SV} (km/s)	v_{SH} (km/s)	v_{PV} (km/s)	v_{PH} (km/s)	η	Q_μ
0.0	1.03	0.00	0.00	1.50	1.50	1.00	9999
5.4	1.03	0.00	0.00	1.50	1.50	1.00	9999
5.4	1.50	0.92	0.92	2.10	2.10	1.00	9999
5.5	1.50	0.92	0.92	2.10	2.10	1.00	9999
5.5	2.83	3.48	3.48	6.27	6.27	1.00	140
16.9	2.83	3.48	3.48	6.27	6.27	1.00	140
16.9	3.28	4.39	4.54	7.91	8.02	0.91	140
51.0	3.28	4.39	4.54	7.91	8.02	0.91	140
51.0	3.35	4.41	4.59	8.00	8.14	0.91	150
89.3	3.35	4.41	4.59	8.00	8.14	0.91	140
89.3	3.35	4.22	4.43	7.89	8.05	0.91	55
165.5	3.35	4.23	4.31	7.99	8.07	0.94	55
165.5	3.35	4.27	4.27	8.03	8.03	1.00	140
407.7	3.66	4.88	4.88	8.97	8.97	1.00	140
407.7	3.76	5.12	5.12	9.36	9.36	1.00	140
520.4	3.87	5.27	5.27	9.76	9.76	1.00	140
520.4	3.88	5.34	5.34	9.77	9.77	1.00	140
664.0	4.02	5.57	5.57	10.22	10.22	1.00	140
664.0	4.35	5.78	5.78	10.66	10.66	1.00	231
761.3	4.42	6.16	6.16	10.94	10.94	1.00	231
761.3	4.44	6.19	6.19	11.02	11.02	1.00	231
771.0	4.44	6.22	6.22	11.05	11.05	1.00	231

^a Models are calculated at a reference frequency of 35 mHz and linearly interpolated between depths. Below the last depth listed, velocities and density are identical to PREM and Q_μ remains constant. Q_κ is set to the PREM value (57 823) throughout the mantle.

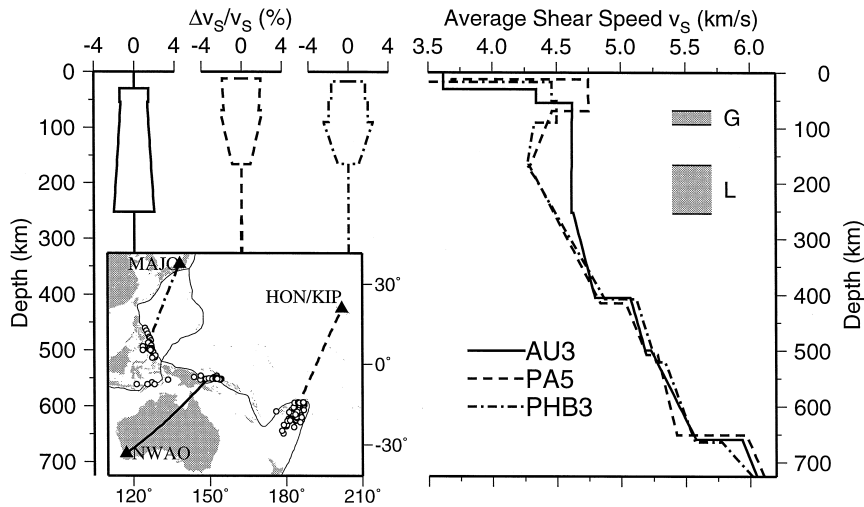


Fig. 4. Shear wave structures for the three regional models discussed in this study. The mean shear speeds ($\bar{v}_S = (v_{SH} + v_{SV})/2$) for AU3 (solid line), PA5 (dashed line), and PHB3 (dash-dotted line) are plotted in the right panel, and the anisotropic deviations about these means ($(v_{SV} - \bar{v}_S)/\bar{v}_S$ and $(v_{SH} - \bar{v}_S)/\bar{v}_S$, in percent) are plotted in the left panels. In all three models, v_{SV} is the slower velocity, v_{SH} is the faster velocity. Depth intervals for the upper mantle discontinuities discussed in the text are shaded: the Gutenberg (G) discontinuity represents the lid/LVZ transition in the oceanic models, and the Lehmann (L) represents the termination of anisotropy, best observed in AU3. The inset map keys the models to the appropriate seismic corridors, including the stations (triangles) and earthquakes (dots) used in the data processing.

S12_WM13. At low frequencies (left panels), both our regional models and those derived by the global tomography match the observations, but at higher frequencies (right panels), the latter show substantial discrepancies. The detailed seismic layering incorporated in the regional models provides an improved capability for calculating the effects of wave propagation through the upper mantle.

2.3. Potential bias due to lateral heterogeneity

In constructing these models, we utilized a path-average approximation, which assumes that the observed waves effectively average heterogeneity between source and receiver, and that the resulting 1-D model represents the average velocity structure along the corridor. The choice of relatively homogenous paths enhances the validity of this approximation, and we further improve the assumption by selectively downweighting observations with substantial sampling outside the regions of interest (the southernmost events in Tonga, or events internal to the Philippine archipelago, for example).

In the case of the Pacific model, we can test this approximation by examining a recent high-resolution, 2-D image of shear velocities along the Tonga–Hawaii corridor. Katzman et al. (1998a) measured an extensive set of travel time data from S, SS, SSS, R_1 , G_1 , and ScS-reverberation phases similar to (but more extensive than) that used in the construction of PA5. These data were inverted using 2-D sensitivity kernels (Zhao and Jordan, 1998), with PA5 as the reference model. The resulting model TH2 displays substantial along-path variability in mean shear velocity ($\pm 2.5\%$), shear wave anisotropy ($\pm 1\%$), and depths to the 410- and 660-km discontinuities (± 10 km) (Katzman et al., 1998a). This lateral heterogeneity does not compromise PA5's representation of the average velocity along the corridor, however. Fig. 6 compares the mean shear speed in PA5 with the along-path average of shear velocities in TH1. The two representations differ negligibly ($< 0.5\%$) throughout the upper mantle and TZ, and similar conclusions can be drawn from comparisons of average discontinuity depth and anisotropy between the two models.

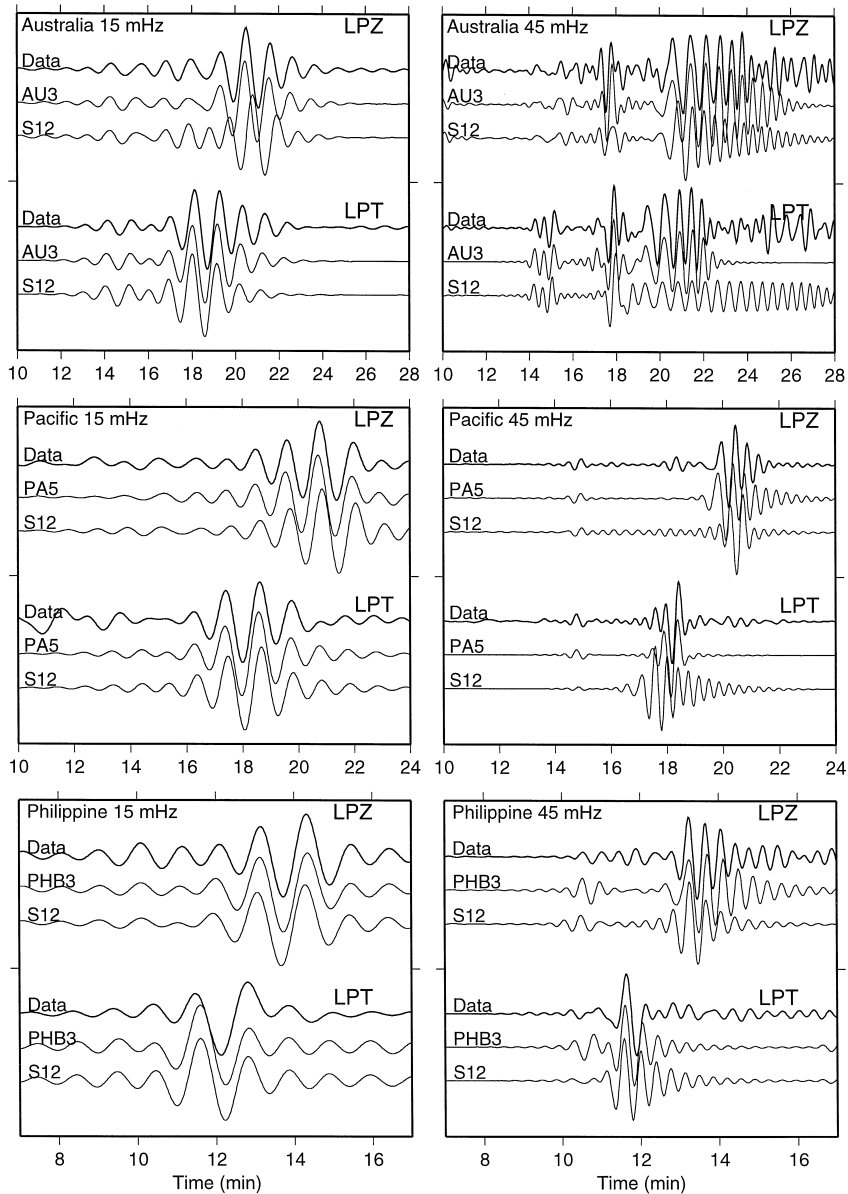


Fig. 5. Comparison of observed seismograms (labeled Data) with synthetics computed from the regional models of Fig. 1 (labeled AU3, PA5, and PHB3) and the tomographic model S12_WM13 of Su et al. (1994) (labeled S12, calculated via perturbation theory of Woodhouse and Dziewonski, 1984). The seismograms are from shallow-focus events recorded at the seismic stations indicated on Fig. 1. They have been low-pass filtered with corners at 15 mHz (left panels) and 45 mHz (right panels).

An additional test comes from comparing two measures of the mean shear velocity contrast between the Philippine Sea basin and the western Pacific in the uppermost mantle. PA5–PHB3 give a

difference of approximately 6%, while a 2-D analysis extending from the Ryuku subduction zone to Hawaii (Katzman et al., 1998b) gives a nearly identical value (5.8%). These tests strengthen our confi-

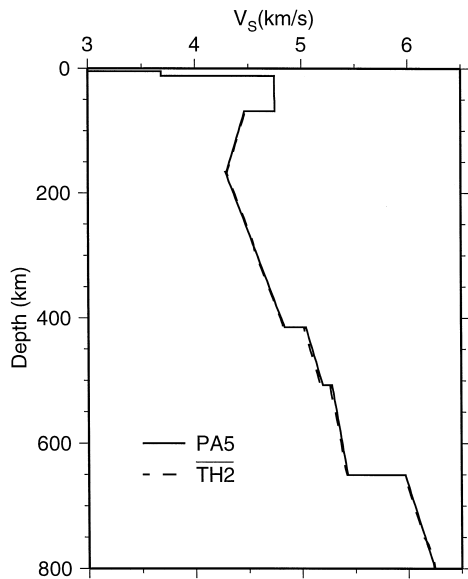


Fig. 6. Comparison of PA5 with the along-path average of the 2-D shear velocity model TH2 of Katzman et al. (1998a).

dence that the path average approximation provides meaningful information for investigating mantle layering in these and other regions.

2.4. Potential bias due to restricted anisotropic parameterization

The apparent splitting between SH and P–SV observations (Fig. 3) is direct evidence for seismic anisotropy in the upper mantle. This anisotropy is most likely related to the lattice-preferred orientation (LPO) of olivine in upper mantle peridotites caused by shearing during plate formation, translation, and deformation, which induces 3-D directional asymmetry in the wave speeds (e.g., Nicolas and Christensen, 1987). A complete description of this anisotropy requires 13 elastic parameters: the five parameters of radial anisotropy, which distinguish vertical and horizontal velocities; and eight additional parameters which describe azimuthal velocity variation (e.g., Montagner and Nataf, 1986). The restriction of our analyses to single-azimuth corridors (which minimizes the impact of lateral heterogeneity) limits us to a radially anisotropic model. This limited parameterization could potentially bias our results.

The magnitude of this bias depends in the length scale over which LPO is coherent, and we consider

two scenarios. The travel times used in our analysis represent integrals of a projection of the 3-D anisotropy onto the direction of wave propagation, with the SH times being dominated by the horizontal velocities, and SV times dominated by vertical velocities. If the local anisotropy varies significantly along the propagation path, then the azimuthal terms average out, and radial anisotropy inferred from these travel times represents an unbiased path average of the media (e.g., Estey and Douglas, 1984; Jordan and Gaherty, 1995). This scenario seems to be appropriate for the geologically complex continental lithosphere in Australia (Gaherty and Jordan, 1995). Alternatively, the local anisotropy may be coherently aligned over distances as large or larger than the corridor lengths. Such a situation may occur in oceanic lithosphere, and in oceanic and continental asthenosphere, where plate-scale anisotropy associated with sea-floor spreading and present-day plate motion has been proposed (e.g., Montagner, 1985; Nicolas and Christensen, 1987; Nishimura and Forsyth, 1989; Montagner and Tanimoto, 1991). For plausible values of local anisotropy (3–8%; Christensen, 1984), the projection of such large-scale horizontal anisotropy onto the propagation path is expected to yield radial anisotropy magnitudes that are positive and large (up to 5%) for paths perpendicular or oblique to the LPO, but small (and even negative) for paths within $\pm 20^\circ$ to this direction (Kawasaki and Kon’no, 1984; Maupin, 1985). The values of the radial anisotropy parameters in our models thus do not represent the true values of these parameters in a complete azimuthal description. We are primarily interested in the depth distribution of anisotropy and its relationship to discontinuities and other structural features of the mantle, however, and in the oblique case, our models provide a robust estimate of these attributes (Maupin, 1985). The subparallel case is problematic for even these general inferences because at such angles a large-scale, coherent anisotropic region could appear isotropic (L  v  que and Cara, 1983; Maupin, 1985).

In our three models, we feel that this latter scenario is unlikely. Our corridors all are oblique or perpendicular to current plate motion (Fig. 1), and thus should be sensitive to anisotropy due to this mechanism. The Philippine path does appear to be nearly parallel to fossil spreading along its southern

half, but we do infer approximately 4% radial shear anisotropy in the lid in this model, and similar values are found on an east–west profile across the basin (Katzman et al., 1998b). The Pacific path has a mean orientation of 50–60° relative to fossil spreading and also has anisotropy of about 4%, consistent with expected values for a sea-floor spreading mechanism (Gaherty et al., 1996). PA5 has proven to be a good average model for subsequent analyses of lateral variations in anisotropy across several Pacific corridors (Katzman et al., 1998a,b; Levin and Park, 1998). Despite these consistencies, however, we retain the caveat that ‘isotropic’ regions of our models could be locally anisotropic, but with alignment that is (a) coherent and roughly parallel to the propagation direction, or (b) incoherent over 3000–4000 km path lengths.

3. Layering in the Earth’s mantle

The corridors in Fig. 1 traverse three distinct, tectonically homogeneous regions, and the corresponding models are representative of the seismic signature of the associated tectonic regimes. The Australia corridor is predominantly characterized by continental crust, specifically a suite of Archean cratons and Proterozoic platforms that were assembled by 1400 Ma, with only minor subsequent internal reactivation (e.g., Rutland, 1981); AU3 is thus a model of a stable continent. The central Pacific path is confined to 100–125 Ma oceanic crust, and PA5 thus represents the upper mantle beneath an old ocean plate. The Philippine Sea corridor crosses the western part of the Philippine Sea plate, primarily the Western Philippine Basin, the Shikoku basin, and the intervening ridges and plateaus. The oceanic crust in these regions appears to be largely of back-arc origin, with an age range of 15–50 Ma (Hall et al., 1995). PHB3 thus characterizes the upper mantle beneath an oceanic plate that is significantly younger than, and has a distinct origin from, that associated with PA5.

We aim to understand the causative mechanisms of four distinctive features of the upper mantle models by considering their regional variability. The first three correspond to depth intervals in the mean shear velocity structure: (1) the velocities and discontinu-

ities associated with the lid and LVZ, between the Moho and approximately 200 km depth; (2) the velocities and gradients between approximately 200 km depth and the 410-km discontinuity; and (3) the TZ, including the 410-, 520-, and 660-km discontinuities. The fourth is represented by the radially anisotropic zone and associated discontinuities, which may correspond to one or more of the above depth intervals.

3.1. Lid, low-velocity zone, and the G discontinuity

The differences among the models in Fig. 4 are largest in the upper 200 km, as observed in other regional studies (Nolet et al., 1994). The two oceanic models are characterized by a high-velocity seismic lid separated from a distinct LVZ by the G discontinuity. In contrast, AU3 has no LVZ in the mean isotropic shear speed; nearly constant lithospheric velocities extend to 250 km depth, and shear velocities in AU3 are resolvably higher than in PA5 to over 300 km depth (Gaherty and Jordan, 1995). The high velocities in AU3 most likely reflect the low temperatures and depleted major-element chemistry associated with the thick tectosphere beneath this ancient continental region (e.g., Jordan, 1978, 1988), and are consistent with previous studies from Australia (Kennett et al., 1994) and other continental regions (Lerner-Lam and Jordan, 1983; Grand and Helmberger, 1984a,b; Lerner-Lam and Jordan, 1987) as well as global tomographic analyses (e.g., Zhang and Tanimoto, 1993; Su et al., 1994). Beneath the oceanic regions, temperatures are higher and more closely approach (or cross) the mantle solidus, leading to a distinct LVZ (Anderson, 1989; Sato et al., 1989).

Further consideration of our oceanic models indicates that temperature is not the sole control on the transition from lid to LVZ, however. The reflection peak for G observed in the ScS reverberation profile for the Philippines was significantly deeper than that observed beneath the Pacific (Revenaugh and Jordan, 1991b), and the surface wave velocities were found to be anomalously low (Kato and Jordan, 1998). These observations required a thicker and slower lid along the Philippine Sea corridor relative to the Pacific. In PA5, the lid is 56 ± 5 km thick with mean shear velocity $\bar{v}_S = 4.75 \pm 0.04$ km/s, whereas in

PHB3, it is 72 ± 6 km thick with a mean velocity $\bar{v}_s = 4.48 \pm 0.05$ km/s (Fig. 4). Since the area sampled in the Philippine Sea is younger than in the Pacific, the increased depth to the G discontinuity is inconsistent with a thermally controlled transition proposed in many previous studies (e.g., Leeds et al., 1974; Anderson and Regan, 1983), which would require a thinning lid with decreasing age. This inference is also supported by the magnitude of the mean shear velocity difference; relative to the Pacific, velocities beneath the Philippine Sea are too low to be explained by thermal differences alone (Kato and Jordan, 1998).

The models are consistent with a scenario where the G in older oceanic regions is a compositional boundary set by the depth of melting during the production of the overlying oceanic crust (Fig. 7). The extraction of basaltic melt at a mid-ocean ridge generates two major compositional changes to the mantle source region: it depletes it of Al, Ca, and Fe relative to Mg (e.g., Ringwood, 1975), and it efficiently strips it of any volatiles (H_2O , CO_2) that are present (Karato, 1986; Hirth and Kohlstedt, 1996). The resulting compositional layering—dry, partially

depleted peridotite residuum underlain by ‘damp’ (hydrous but undersaturated) fertile peridotite—persists as the plate translates away from the ridge. The major-element depletion increases the shear velocity by less than 1% (e.g., Fig. 8 in the work of Jordan (1979)), but the volatile contrast could result in a larger seismic discontinuity (Karato, 1995). By considering the likely quantities and solubility of volatiles in oceanic upper mantle, Hirth and Kohlstedt (1996) estimated that the damp peridotite will be two orders of magnitude less viscous than the overlying dry harzburgite owing to the water-enhanced defect mobility in olivine. Because defect mobility also controls seismic Q , which in turn has an indirect effect on seismic velocities, Karato (1995) suggested that the presence of water can reduce seismic velocities by several percent. Building on these arguments, we hypothesize that G represents the seismic signature of the relatively abrupt transition from drier to more damp peridotite, and that it is coincident with a sharp drop in Q (Tables 2 and 3) and viscosity (Hirth and Kohlstedt, 1996). This hypothesis explains several aspects of our regional velocity structures: the magnitude of the velocity drop (3–6%) is consistent with the mechanism predicted by Karato (1995) assuming the water content estimated by Hirth and Kohlstedt (1996); the range of depth of the dry-to-wet transition predicted by Hirth and Kohlstedt (1996) is compatible with the depth of G in PA5 and PHB3; and the abrupt transition from wet to dry can explain the sharpness of the seismic transition (constrained by ScS reverberations to be less than 30-km width). The scenario is similar to that recently proposed by Karato and Jung (1998) to explain the seismic observations of Revenaugh and Jordan (1991b) and Gaherty et al. (1996).

The association of G with the depth of melting suggests that melting initiated deeper beneath the western part of Philippine Sea plate than beneath the central Pacific (89 vs. 68 km depth, respectively). This implication is testable, because an increase in depth to melting should correspond to an increase in crustal thickness due to the larger volume of the melt column. As shown in Fig. 8, the crust in PHB3 (11.5 ± 1.5 km) is significantly thicker than that in PA5 (6.8 ± 1.0 km), in qualitative agreement with this prediction. We evaluate the apparent correlation between crustal thickness and depth to G (melting)

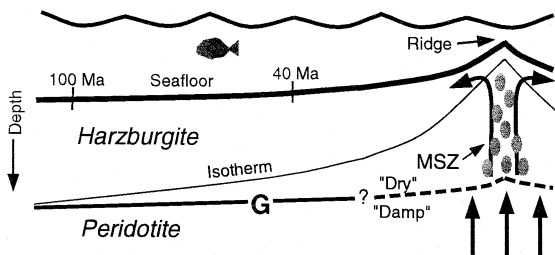


Fig. 7. Schematic cross-section of oceanic upper mantle, depicting the compositional layering hypothesized to give rise to the G discontinuity. Decompression melting and extraction of basaltic magma occurs in a narrow melt separation zone (MSZ) beneath the ridge crest. Any volatiles present in the mantle source region will enter the melt phase, resulting in a dry layer of depleted peridotite residuum overlying water-undersaturated (‘damp’) normal mantle. This compositional boundary is preserved as the plate ages. We argue that far from the partially molten near-ridge environment, this contrast in volatile content is responsible for the observed G discontinuity, and as such it represents the fossilized base of the MSZ. One prediction of this model is that the depth to G should be relatively constant for a given ocean basin far from the ridge (thick solid line). For comparison, if G corresponds to a critical isotherm (thin line), then its depth should increase with plate age.

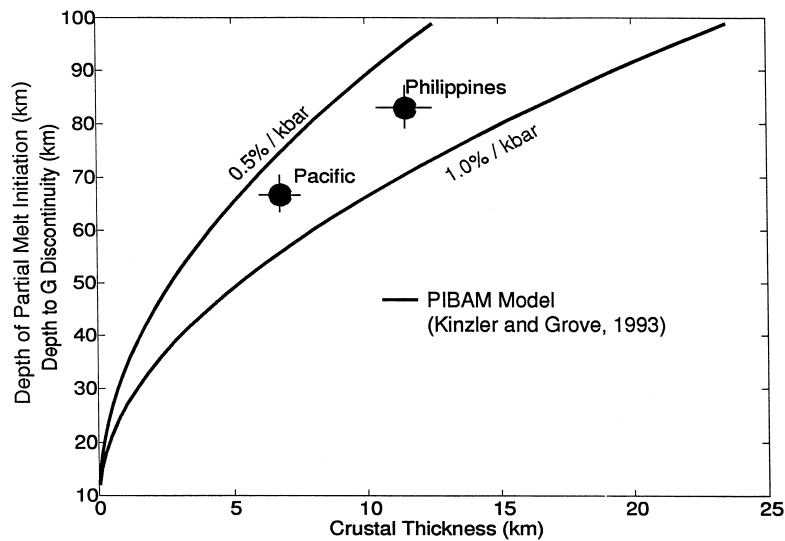


Fig. 8. Observed depth to the G discontinuity in PA5 and PHB3, plotted against the path averaged crustal thickness found in these models. Also plotted are curves for a simple polybaric, incremental batch, accumulative melting (PIBAM) model, after the work of Kinzler and Grove (1993). In this melting model, crustal thickness is a function of depth of initiation of melting, with average rate of melt generation being a free parameter. Our observed correlation between crustal thickness and depth to melt initiation corresponds to plausible (0.5–1.0%/kbar) average melting rates.

quantitatively by comparing it with that predicted for a simple incremental, polybaric, near-fractional melting model (Kinzler and Grove, 1993). In this model, melting is initiated at a chosen depth (pressure), and it proceeds at a constant rate (0.5 and 1.0%/kbar of ascent for the two curves in Fig. 8), with 90% of the melt being removed with each ascending step. Melting terminates at 12 km depth, and the predicted crustal thickness is a smooth function of the initial depth of melting (Fig. 8). This model is a gross simplification of melt generation in the near-ridge environment; it ignores the likely functional dependence of melting rates and melt retention on pressure, temperature, and water content, for example (e.g., McKenzie and Bickle, 1988; Plank and Langmuir, 1992). The discontinuity depths in our seismic models can be matched by such a model with an average melting rate of approximately 0.7%/kbar, however, and while we do not place any significance in this specific value, it implies that the association of G with initial depth of melting is petrologically plausible.

An increase in the depth to melting beneath the ancient Philippine Sea ridge environment (relative to the ancient Pacific) could be accomplished via one

of two mechanisms: a lowering of the melting temperature due to increased water content, or an increase in temperature. There is evidence for the former; relatively high vesicularity and alkalinity of basaltic rocks drilled from the northwestern portion of the Philippine Sea plate (which our corridor traverses) are consistent with increased water content and deeper melting within the ancient source region (Dick, 1982). The long history of subduction surrounding the Philippine Sea plate (Hall et al., 1995) provides a source of the extra water.

This hypothesis implies that there should be little age-dependence in the depth to G within the stable (non-ridge) portion of an oceanic plate (Fig. 7). This prediction is in contrast with previous inferences regarding the Pacific upper mantle, which indicate a steady increase of seismic lid thickness with increasing plate age due to thermal cooling (Leeds et al., 1974; Anderson and Regan, 1983; Montagner and Jobert, 1983). Such models result solely from the inversion of fundamental-mode surface wave data, which have poor resolution of lid thickness (Nishimura and Forsyth, 1989). Direct observations of reflections and/or conversions from the G discontinuity (e.g., Revenaugh and Jordan, 1991b; Bock,

1991) are required to unambiguously determine lid thickness, and we have utilized such observations here.

3.2. Velocity gradients between 200 and 400 km depth

Unlike PREM and some previous models from these regions (Kanamori and Abe, 1968; Schlue and Knopoff, 1977; Mitchell and Yu, 1980; Anderson and Regan, 1983), our models do not have low-velocity channels with a sharp lower boundary. PHB3 and PA5 smoothly transition from a minimum velocity near 170 km depth into a high-gradient zone (HGZ) that extends to the 410 discontinuity. The similarity of the velocities in the HGZ in PA5 and PHB3 implies that the differences in thermal structure and/or volatile content responsible for the low lid/LVZ velocities in PHB3 are confined above 200 km depth. This steep gradient can be found in several other oceanic models (Fig. 9), and it contrasts

sharply with the relatively flat gradient found in AU3 and many continental models (Fig. 9) within this depth interval. The HGZ thus appears to be governed by the thermal structure of the convecting oceanic upper mantle, but it is intriguing in that it cannot be accounted for as a simple adiabatic increase of velocity and density for plausible mantle mineralogies (e.g., Ita and Stixrude, 1992).

The HGZ most likely results from near-solidus conditions at the base of the LVZ in stable oceanic regions. The geotherm $T(z)$ in this convecting region should approximate an adiabat with a gradient of about 0.3 K/km (Ita and Stixrude, 1992), while the solidus temperature $T_m(z)$ for mantle peridotites has a significantly steeper gradient, on the order of 1.0 K/km or greater (Thompson, 1992). The homologous temperature T/T_m therefore will decrease by of order 10% across the HGZ (Fig. 10). If the mantle adiabat approaches the mantle solidus at the top of the HGZ (i.e., $T/T_m > 0.9$), then $dV_S/d(T/T_m)$ may be sufficiently large (e.g., Sato et al., 1989) to

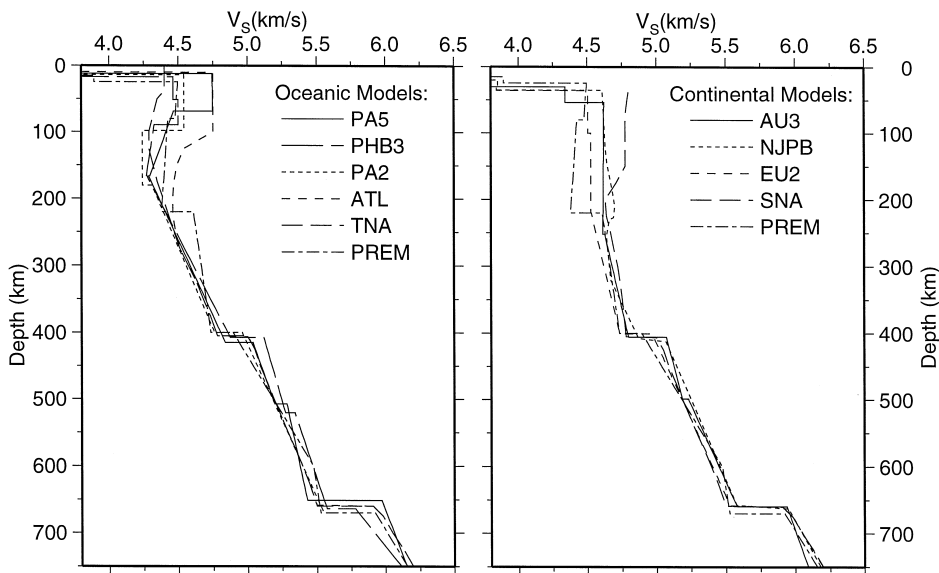


Fig. 9. Mean isotropic shear velocity profiles for AU3, PA5, and PHB3, plotted with other regional oceanic (left panel) and continental (right panel) models, as well as PREM. The oceanic models are characterized by a high-velocity lid, a distinct LVZ (with velocities generally on the order of 4.3–4.4 km/s), and a HGZ extending from near 200 km to the 410 discontinuity. The 220-km discontinuity and underlying flat-gradient region in PREM is clearly in marked disagreement with the HGZ in the oceanic models. In contrast, the continental models have high velocities extending throughout the upper mantle—even those such as SNA that have velocity reversals with depth (indicating an apparent LVZ) never have velocities lower than 4.5–4.6 km/s, significantly higher than those found in the LVZ in the oceanic models. In addition, these models have a much flatter gradient between 200 km depth and the 410, in very good agreement with PREM. References for models: PA2 and EU2, Lerner-Lam and Jordan (1987); SNA and TNA, Grand and Helmberger (1984a); ATL, Grand and Helmberger (1984b); NJPB, Kennett et al. (1994); PREM, Dziewonski and Anderson (1981).

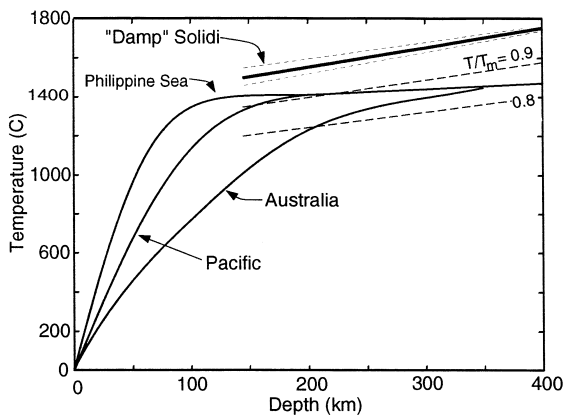


Fig. 10. Comparison of an estimated 'damp' solidus for pyrolite with model geotherms for our three seismic corridors. Solidus is constructed using the melting temperature T_m of pyrolite by Hirth and Kohlstedt (1996) with a water content of $815 \text{ H}/10^6 \text{ Si}$ at 180 km depth, and then extrapolating to greater depth assuming a gradient of 1.0 K/km (bold line). Short-dashed lines represent bounding water contents of $\pm 440 \text{ H}/10^6 \text{ Si}$, and long-dashed lines are contours of constant homologous temperature (T/T_m). The oceanic geotherms assume a cooling half-space with a potential temperature of 1450°C , merging into a mantle adiabat with a gradient of 0.3 K/km (Ita and Stixrude, 1992). The Australia geotherm is the 40 mW/m^2 geotherm of Pollack and Chapman (1977).

explain the high shear velocity gradient. This model is consistent with the lower gradients beneath Australia; assuming the thickness of the thermal boundary layer is on the order of 300–400 km, the change in T/T_m for a continental geotherm (e.g., Pollack and Chapman, 1977) will be small over this depth interval, and thus velocity will increase only slowly (Fig. 10).

3.3. Transition zone

In the TZ, the Pacific model is slow, with a deep 410-km discontinuity ($415 \pm 3 \text{ km}$) and a shallow 660-km discontinuity ($651 \pm 4 \text{ km}$). At the other extreme, the Philippine Sea model has a fast TZ, with a shallow 410 ($408 \pm 3 \text{ km}$) and deep 660 ($664 \pm 3 \text{ km}$). This relative behavior of discontinuity depths and TZ velocities is in general agreement with calculated Clapeyron slopes of phase changes in an olivine-dominated mantle; positive for the α – β transition in olivine at 410, and negative for the γ – $\text{Pv} + \text{Mw}$ (perovskite plus magnesiowüstite)

transition at 660 (e.g., Bina, 1991). All three models were constructed to provide good matches to the bulk sound velocity and density profiles of pyrolite (Ita and Stixrude, 1992) throughout the TZ. On average, the TZ beneath Australian corridor seems to be slightly cooler than that beneath the Pacific corridor, in agreement with observed correlation between thickened (and therefore low-temperature) TZ and old continents by Gossler and Kind (1996). The Philippine Sea TZ is even colder, consistent with previous studies (Masters et al., 1982; van der Hilst et al., 1991; Fukao et al., 1992; Brudzinski et al., 1997). The low temperatures are perhaps due to the presence of cooler material advected downward in the surrounding subduction zones.

All three models contain small 520-km discontinuities, primarily to satisfy the ScS reverberation data. The 520 appears to be a global feature (Shearer, 1990; Revenaugh and Jordan, 1991a) most likely caused by the broad (30-km width) β – γ transition in $(\text{Mg}, \text{Fe})_2\text{SiO}_4$ (Akaogi et al., 1989), with a possible contribution from the exsolution of calcium perovskite (Gasparik, 1990; Bina, 1991). The velocity and density contrasts that we obtain for this discontinuity are consistent with the available mineralogical data (Bina, 1991; Rigden et al., 1991). Due to its small size relative to the 410 and 660, the depth of the 520 is difficult to constrain from the ScS reverberation profiles, and thus the depth variation of this feature among the models is probably not significant (in all models, this depth has a standard error of at least $\pm 10 \text{ km}$).

Fig. 4 displays very large differences in the shear-speed magnitude of the 660-km discontinuity between the three regions. Some of this difference may be attributable to deficiencies in our models at this depth. We restricted our parameterization to a single layer below 660, and required the velocities at the base of this layer to match those in PREM. This effectively forces the layer to absorb any velocity differences sensed by the direct S waves, which turn between the 660 and approximately 1000 km depth. As a result, overly large differences in shear velocity and density may have been introduced between the models in this depth interval. This is most apparent in the contrast between PHB3 and AU3, which have nearly identical values of shear impedance (product of shear velocity and density) across 660, but almost

a factor of two difference in velocity and density jumps (Fig. 4, Tables 1 and 3).

Nevertheless, part of this difference is required by the data. The shear impedance of 660-km in the three models is well-constrained by the ScS reverberation data, and it varies systematically with depth of the reflector; the relatively deep 660 in PHB and AU3 are 30% smaller than the shallower (by ~ 10 km) 660 in PA5. A similar trend was noted by Revenaugh and Jordan (1991a), who were unable to come up with a satisfactory explanation. One possibility is that it is due to the multi-component aspect of the discontinuity. In a pyrolite mantle, two distinct, coupled phase transitions will occur near 660-km depth: the endothermic $\gamma - \text{Pv} + \text{Mw}$ transformation, which occurs over an extremely narrow (1–5 km) depth interval; and the exothermic garnet–Pv transition, which takes place over a wider (30–60 km) depth range (Ita and Stixrude, 1992; Weidner and Wang, 1998). The combination of the two results in complex velocity and density increases, even for a single-composition (e.g., pyrolite) mantle, and the form and sharpness of the transition is a strong function of temperature (Weidner and Wang, 1998). Initial calculations indicate that the variability in 660 observed in our models can be explained by these coupled phase transitions in a pyrolite mantle. Such a model has the additional benefit of explaining why long-period data such as ScS reverberations indicate a large 660 discontinuity, while higher frequency observations (to which the garnet change would not appear so discontinuous) often require a smaller discontinuity (e.g., Walck, 1984). A distributed garnet transition also can explain the increased gradient sometimes observed just above and/or below 660 in some models (Walck, 1984; Brudzinski et al., 1997; Estabrook and Kind, 1996; Vinnik et al., 1997).

3.4. Anisotropic zone and the *L* discontinuity

Radial anisotropy is continuous throughout the uppermost mantle in all three regions. Its presence is required by the differential travel times (splitting) between horizontally polarized (SH) and vertically polarized (SV) shear waves. SH waves were always observed to be faster than SV waves, which requires ‘normal’ radial anisotropy ($v_{\text{SH}} > v_{\text{SV}}$, $v_{\text{PH}} > v_{\text{PV}}$). Anisotropy of this type is most plausibly related to

the LPO of olivine with fast axes aligned roughly horizontal (e.g., L  v  que and Cara, 1983; Jordan and Gaherty, 1995). In the oceans, this alignment corresponds to the directions of past and present sea-floor spreading (e.g., Nicolas and Christensen, 1987; Nishimura and Forsyth, 1989), while in the continents, the upper mantle anisotropy appears to be inherited from episodes of horizontal shearing during orogenic deformation (Mainprice and Silver, 1993; Silver, 1996). In all three of our regions, the data were satisfied by models with an average shear anisotropy ratio $\Delta v_{\text{S}}/\bar{v}_{\text{S}} = 2(v_{\text{SH}} - v_{\text{SV}})/(v_{\text{SH}} + v_{\text{SV}})$ of 3–4%, extending from the Moho to near 200 km depth.

The depth extent of the anisotropy was constrained by the relative magnitude of observed splitting in different wave types (Fig. 3). The largest splitting was observed in surface waves (the Love–Rayleigh discrepancy), requiring anisotropy in the shallowest portions of the mantle, above 200 km depth (Gaherty and Jordan, 1995; Gaherty et al., 1996). Splitting was observed in SSS and SS waves that turn deeper in the upper mantle and TZ, but it was smaller than that found in the surface waves, and it was unresolvable in S waves that turn in the TZ and lower mantle. This falloff in splitting strongly limits the depth extent of the path average radial anisotropy. In particular, because SS and SSS phases are sensitive to shallow anisotropy as well as anisotropy near their turning points deeper in the mantle, splitting in such phases can be explained by the radial anisotropy needed to satisfy the surface wave splitting (Fig. 11), and any additional radial anisotropy at larger depths must be smaller than 1%. As noted in Section 2.4, our radial models do not preclude azimuthal anisotropy at depths greater than 250 km (e.g., Montagner and Tanimoto, 1991; Tong et al., 1994; Montagner and Kennett, 1996), but such anisotropy must either be aligned roughly parallel to the propagation paths, or it must be variable in dip as well as azimuth such as to integrate to isotropy over the path length.

As an example of this depth sensitivity, our data from Australia are not consistent with models invoking a predominantly isotropic lithosphere underlain by a layer of anisotropy associated with plate motion-induced shear at its base (i.e., between 200–400 km depth), as has been advocated beneath Australia

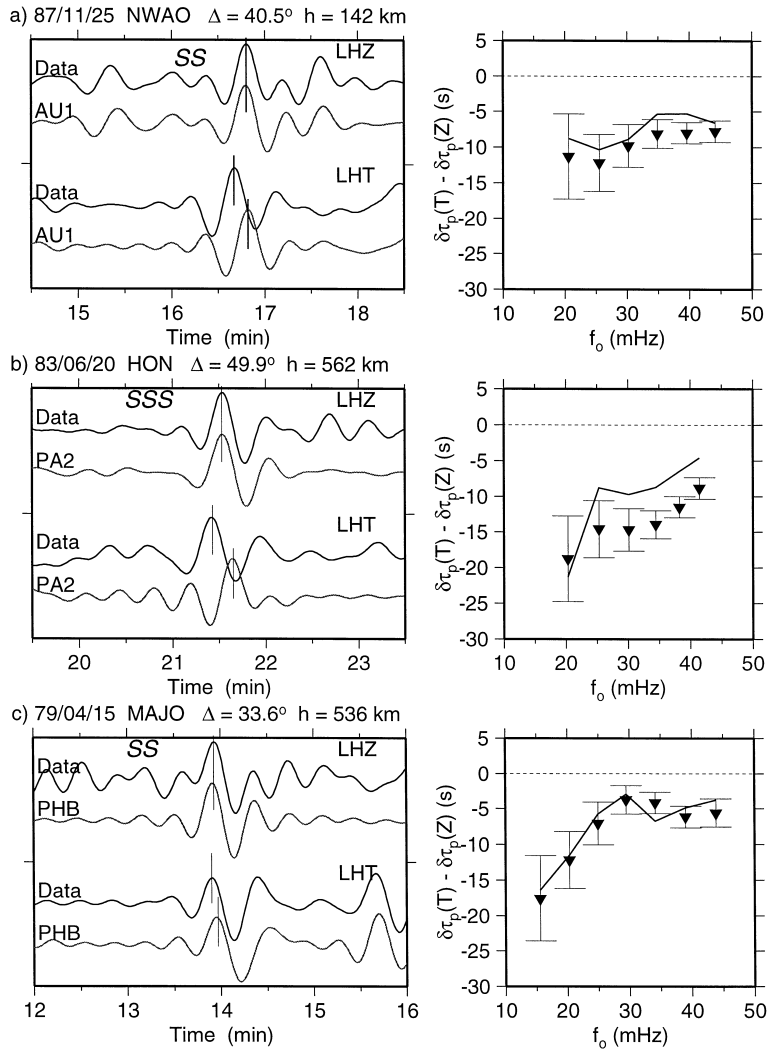


Fig. 11. Examples of clear, distinctive splitting of SS and SSS body waves by upper mantle anisotropy. (a) Splitting of a SS wave that traversed the Australia corridor. (b) Splitting of a SSS wave that traversed the Pacific corridor. (c) Splitting of a SS wave that traversed the Philippine Sea corridor. Left panels display examples of long-period seismograms centered on the SS or SSS arrival, band-passed between 5–45 mHz. Each panel includes observed vertical- and transverse records, along with complete normal-mode synthetics for an isotropic starting model, aligned on the LHZ SS (or SSS) arrival. In all three cases, the peak of the SS or SSS arrival on LHT is significantly advanced relative to the isotropic model, by 4–12 s. Right panels quantify the splitting in these waveforms. Symbols display the differences between the tangential phase delays $\delta\tau_p(T)$ and the vertical phase delays $\delta\tau_p(Z)$ at each frequency, relative to the prediction of the isotropic starting models (dashed lines). Solid lines represent the fit of models AU3, PA5, and PHB3 to these individual observations.

(Leven et al., 1981; Tong et al., 1994) and elsewhere (Vinnik et al., 1992, 1995). Enforcing an isotropic continental lithosphere prevented us from fitting the surface waves, and maintaining the fit to the SS and S splitting while introducing sufficient shallow anisotropy to satisfy the surface waves limited the

deeper average anisotropy to less than 1%. Adding even 1% radial shear anisotropy to AU3 between 250- and 400-km depth anisotropy would increase the average SS splitting by approximately 3 s, which does not match the observations. To be consistent with this result, the LPO associated with plate mo-

tion-induced shear between 250–400 km must be very weak, or it must be roughly parallel to the propagation path, at a 30–40° angle to Australia's predicted motion in a hotspot reference frame (Fig. 1).

In AU3, radial anisotropy terminates rather sharply across the L discontinuity, and we have investigated this phenomenon in some detail (Gaherty and Jordan, 1995). The presence of high velocities throughout the anisotropic layer in this model implies that the anisotropy is related to small-scale tectonic fabric generated in episodes of orogenic compression associated with tectospheric stabilization (Silver and Chan, 1991), rather than active flow in the asthenosphere (Karato, 1992). Below L, such structures were either annealed out subsequent to their formation (Revenaugh and Jordan, 1991b), or were never generated, perhaps because L coincides with a transition from dislocation to diffusion creep (Karato, 1992) or because of an increase in the relative amount of vertical deformation. The L discontinuity is located near the maximum depth of equilibration observed for suites of kimberlite xenoliths from several continental cratons, which averages approximately 220 km (Finnerty and Boyd, 1987). This equilibration level is interpreted to be the transition from slow diapiric upwelling of kimberlite magmas (or their precursors) (Green and Gueguen, 1974) to much more rapid upward transport by magma fracturing through a stronger lithosphere (Spence and Turcotte, 1990). The L discontinuity may thus correspond to the base of a mechanical boundary layer that overlies a more mobile, dynamically active part of the continental tectosphere. The transition also appears to correspond to an abrupt downward increase in shear wave attenuation observed at about this depth (Table 1; Gudmundsson et al., 1994).

The termination of anisotropy in PA5 and PHB3 also occurs at L, but this boundary is poorly defined in these models because it is not large enough to be observed in the reverberative profiles for these two paths (Revenaugh and Jordan, 1991b). The data did require a reduction of the radial anisotropy near the transition from negative to positive velocity gradient in the LVZ, however, and allowing a small ($< 1\%$, undetectable to ScS reverberations) L discontinuity accommodated this reduction with the minimal number of model parameters. The drop in average anisotropy

in PA5 and PHB3 could correspond to the bottom of the zone of coherent horizontal shear (either fossilized or active) or to a change from dislocation-dominated to diffusion-dominated creep within the shear zone, as suggested by Karato (1992).

4. Conclusions

We present a systematic analysis of the lateral variability of mantle layering using three new regional seismic models. From this analysis we hypothesize that: (1) the LVZ is predominantly an oceanic feature associated with high (near-solidus) homologous temperatures in the shallow oceanic upper mantle. The sharp transition from lid to LVZ is predominantly determined by an increase in water content in the LVZ. (2) Shear velocity gradients between 200–400 km depth are significantly steeper beneath oceans than continents, due to the rapid drop in homologous temperature across this depth interval in oceanic environments. (3) Regional variability of the TZ velocities and discontinuities are consistent with a pyrolite mantle. (4) When averaged over 30–40° paths, strong seismic anisotropy ($> 1\%$) is restricted to the upper 200–300 km of the upper mantle. In stable continents this anisotropy is relegated to the cold, mechanically stiff layer above the L discontinuity, while in oceans it extends through the lid into the LVZ.

These hypotheses regarding the mechanical, phase, and compositional layering of the mantle are not resolvable in the current generation of global models. Indeed, comparing Figs. 2 and 4 indicates that regional models such as these provide significant information on lateral heterogeneity that is complementary to that provided by tomographic models.

Our ability to fully test many of these hypotheses is restricted by the limitation of our 1-D modeling to regions of minimal tectonic complexity. For example, how exactly does the LVZ disappear in the transition from a PA5-like structure to an AU3-like structure across an ocean-continent boundary? Such a question can only be answered with 2-D and 3-D tomographic analyses that include lateral variability of velocities, discontinuities, and anisotropy (Katzman et al., 1998a,b). Building on AU3, PA5, and PHB3 as reference models, such analyses should

greatly expand our understanding of seismic layering in the near future.

Acknowledgements

We thank the Harvard and IRIS data centers for their assistance in collecting digital seismograms; R. Katzman for the TH2 path averages used in Fig. 7 and helpful discussions; and T. Grove, G. Hirth, S. Karato, P. Puster, Y. Wang, and D. Weidner for useful discussions. G. Ekstrom and J.-P. Montagner provided thorough reviews that led to substantial improvement of the manuscript. Several figures were generated using the free software GMT (Wessel and Smith, 1995). This research was supported by the Defense Special Weapons Agency under grant F49620-95-1-0051, and the National Science Foundation under grant EAR-94-18439.

References

- Akaogi, M., Ito, E., Navrotsky, A., 1989. Olivine-modified spinel–spinel transitions in the system $\text{Mg}_2\text{SiO}_4\text{--Fe}_2\text{SiO}_4$: calorimetric measurements, thermochemical calculation, and geophysical application. *J. Geophys. Res.* 94, 15671–15685.
- Anderson, D.L., 1989. *Theory of the Earth*. Blackwell, Boston, MA.
- Anderson, D.L., Regan, J., 1983. Upper mantle anisotropy and the oceanic lithosphere. *Geophys. Res. Lett.* 10, 841–844.
- Bina, C.R., 1991. Mantle discontinuities: US Natl. Rep. Int. Union Geodyn. *Geophys.* 1987–1990. *Rev. Geophys.* 29, 783–793.
- Bock, G., 1991. Long-period S to P converted waves and the onset of partial melting beneath Oahu, Hawaii. *Geophys. Res. Lett.* 18, 869–872.
- Brudzinski, M.R., Chen, W.-P., Nowack, R.L., Huang, B.-S., 1997. Variations of P wave speeds in the mantle transition zone beneath the northern Philippine Sea with implications on mantle dynamics. *J. Geophys. Res.* 102, 11815–11827.
- Christensen, N.I., 1984. The magnitude, symmetry, and origin of upper mantle anisotropy based on fabric analyses of ultramafic tectonites. *Geophys. J. R. Astron. Soc.* 76, 89–111.
- Dick, H.J.B., 1982. The petrology of two back-arc basins in the northern Philippine Sea. *Am. J. Sci.* 282, 644–700.
- Dziewonski, A.M., Anderson, D.L., 1981. Preliminary reference Earth model. *Phys. Earth Planet. Int.* 25, 297–356.
- Estabrook, C.H., Kind, R., 1996. The nature of the 660-km upper mantle seismic discontinuity from precursors to the PP phase. *Science* 274, 1179–1182.
- Estey, L.H., Douglas, B.J., 1984. Upper mantle anisotropy: a preliminary model. *J. Geophys. Res.* 91, 11393–11406.
- Finnerty, A.A., Boyd, F.R., 1987. Thermobarometry for garnet peridotites: basis for the determination of thermal and compositional structure of the upper mantle. In: Nixon, P.H. (Ed.), *Mantle Xenoliths*. Wiley-Interscience, Chichester, pp. 381–402.
- Fukao, Y., Obayashi, M., Inoue, H., Nenbai, M., 1992. Subducting slabs in the mantle transition zone. *J. Geophys. Res.* 97, 4809–4822.
- Gaherty, J.B., Jordan, T.H., 1995. Lehmann discontinuity as the base of an anisotropic layer beneath continents. *Science* 268, 1468–1471.
- Gaherty, J.B., Jordan, T.H., Gee, L.S., 1996. Seismic structure of the upper mantle in a central Pacific corridor. *J. Geophys. Res.* 101, 22291–22309.
- Gasparik, T., 1990. Phase relations in the transition zone. *J. Geophys. Res.* 95, 15751–15769.
- Gee, L.S., Jordan, T.H., 1992. Generalized seismological data functionals. *Geophys. J. Int.* 111, 363–390.
- Gossler, J., Kind, R., 1996. Seismic evidence for very deep roots of continents. *Earth Planet. Sci. Lett.* 138, 1–13.
- Grand, S.P., Helmberger, D.V., 1984a. Upper mantle shear structure of North America. *Geophys. J. R. Astron. Soc.* 76, 399–438.
- Grand, S.P., Helmberger, D.V., 1984b. Upper mantle shear structure beneath the northwest Atlantic Ocean. *J. Geophys. Res.* 89, 11465–11475.
- Green, H.W., Gueguen, Y., 1974. Origin of kimberlite pipes by diapiric upwelling in the upper mantle. *Nature* 249, 617–620.
- Gripp, A.E., Gordon, R.G., 1990. Current plate velocities relative to the hotspots incorporating the NUVEL-1 global plate motion model. *Geophys. Res. Lett.* 17, 1109–1112.
- Gudmundsson, O., Kennett, B.L.N., Goody, A., 1994. Broad-band observations of upper mantle seismic phases in northern Australia and the attenuation structure in the upper mantle. *Phys. Earth Planet. Int.* 84, 207–226.
- Hall, R., Fuller, M., Ali, J., Anderson, C.D., 1995. The Philippine Sea plate: magnetism and reconstructions. In: Taylor, B., Natland, J. (Eds.), *Active Margins and Marginal Basins of the Western Pacific*. Geophysical Monograph 68. American Geophysical Union, Washington, DC, pp. 371–404.
- Hirth, G., Kohlstedt, D.L., 1996. Water in the oceanic upper mantle: implications for rheology, melt extraction, and the evolution of the lithosphere. *Earth Planet. Sci. Lett.* 144, 93–108.
- Ita, J., Stixrude, L., 1992. Petrology, elasticity, and composition of the mantle transition zone. *J. Geophys. Res.* 97, 6849–6866.
- Jordan, T.H., 1978. Composition and development of the continental tectosphere. *Nature* 274, 544–548.
- Jordan, T.H., 1979. Mineralogies, densities, and seismic velocities of garnet lherzolites and their geophysical implications. In: Boyd, F.R., Meyer, H.O.A. (Eds.), *The Mantle Sample: Inclusions in Kimberlites and Other Volcanics*. American Geophysical Union, Washington, DC, pp. 1–14.
- Jordan, T.H., 1988. Structure and formation of the continental tectosphere. *J. Petrol. Special Lithosphere Issue*, 11–37.
- Jordan, T.H., Gaherty, J.B., 1995. Stochastic modeling of small-scale, anisotropic structures in the continental upper mantle.

- Proceedings of the 17th Annual Seismic Research Symposium, PL-TR-95-2108. Phillips Laboratory, MA, pp. 433–451.
- Kanamori, H., Abe, K., 1968. Deep structure of island arcs as revealed by the surface waves. *Bull. Earthquake Res. Inst. Univ. Tokyo* 86, 1001–1025.
- Karato, S.-I., 1986. Does partial melting reduce the creep strength of the upper mantle. *Nature* 319, 309–310.
- Karato, S.-I., 1992. On the Lehmann discontinuity. *Geophys. Res. Lett.* 19, 2255–2258.
- Karato, S.-I., 1995. Effects of water on seismic wave velocities in the upper mantle. *Proc. Jpn. Acad., Ser. B* 71, 61–66.
- Karato, S.-I., Jung, H., 1998. Water, partial melting and the origin of the seismic low-velocity and high attenuation zone in the upper mantle. *Earth Planet. Sci. Lett.* 157, 193–207.
- Kato, M., Jordan, T.H., 1998. Seismic structure of the upper mantle beneath the western Philippine Sea. *Phys. Earth Planet. Int.*, in press.
- Katzman, R., Zhao, L., Jordan, T.H., 1998a. High-resolution, 2-D vertical tomography of the central-Pacific mantle using ScS reverberations and frequency-dependent travel times. *J. Geophys. Res.* 103, 17933–17971.
- Katzman, R., Zhao, L., Jordan, T.H., 1998b. Seismic structure of the mantle between Ryukyu and Hawaii: implications for the Hawaiian swell. *J. Geophys. Res.*, submitted.
- Kawasaki, I., Kon'no, F., 1984. Azimuthal anisotropy of surface waves and the possible type of the seismic anisotropy due to preferred orientation of olivine in the uppermost mantle beneath the Pacific Ocean. *J. Phys. Earth* 32, 229–244.
- Kennett, B.L.N., Gudmundsson, O., Tong, C., 1994. The upper mantle S and P velocity structure beneath northern Australia from broad-band observations. *Phys. Earth Planet. Int.* 86, 85–98.
- Kinzler, R.J., Grove, T.L., 1993. Corrections and further discussion of the primary magmas of mid-ocean ridge basalts, 1 and 2. *J. Geophys. Res.* 98, 22339–22347.
- Leeds, A.R., Knopoff, L., Kausel, E.G., 1974. Variations in upper mantle structure under the Pacific Ocean. *Science* 186, 141–143.
- Lerner-Lam, A.L., Jordan, T.H., 1983. Earth structure from fundamental and higher-mode waveform analysis. *Geophys. J. R. Astron. Soc.* 75, 759–797.
- Lerner-Lam, A.L., Jordan, T.H., 1987. How thick are the continents? *J. Geophys. Res.* 92, 14007–14026.
- Leven, J.H., Jackson, I., Ringwood, A.E., 1981. Upper mantle seismic anisotropy and lithospheric decoupling. *Nature* 289, 234–239.
- Lévesque, J.J., Cara, M., 1983. Long-period Love wave overtone data in North America and the Pacific Ocean: new evidence for upper mantle anisotropy. *Phys. Earth Planet. Int.* 33, 164–179.
- Levin, V., Park, J., 1998. Quasi-Love phases between Tonga and Hawaii: observations, simulations, and explanations. *J. Geophys. Res.*, in press.
- Mainprice, D., Silver, P.G., 1993. Interpretation of SKS waves using samples from the subcontinental lithosphere. *Phys. Earth Planet. Int.* 78, 257–280.
- Masters, G., Jordan, T.H., Silver, P.G., Gilbert, J.F., 1982. Aspherical Earth structure from fundamental spheroidal-mode data. *Nature* 298, 609–613.
- Maupin, V., 1985. Partial derivatives of surface wave phase velocities for flat anisotropic models. *Geophys. J. R. Astron. Soc.* 83, 379–398.
- McKenzie, D., Bickle, M.J., 1988. The volume and composition of melt generated by extension of the lithosphere. *J. Petrol.* 29, 625–679.
- Mitchell, B.J., Yu, G., 1980. Surface wave dispersion, regionalized velocity models, and anisotropy of the Pacific crust and upper mantle. *Geophys. J. R. Astron. Soc.* 63, 497–514.
- Montagner, J.-P., 1985. Seismic anisotropy of the Pacific Ocean inferred from long-period surface waves dispersion. *Phys. Earth Planet. Int.* 38, 28–50.
- Montagner, J.-P., Jobert, N., 1983. Variation with age of the deep structure of the Pacific Ocean inferred from very long-period Rayleigh wave dispersion. *Geophys. Res. Lett.* 10, 273–276.
- Montagner, J.-P., Kennett, B.L.N., 1996. How to reconcile body wave and normal-mode reference Earth models. *Geophys. J. Int.* 125, 229–248.
- Montagner, J.-P., Nataf, H.C., 1986. A simple method for inverting the azimuthal anisotropy of surface waves. *J. Geophys. Res.* 91, 511–520.
- Montagner, J.-P., Tanimoto, T., 1991. Global upper mantle tomography of seismic velocities and anisotropy. *J. Geophys. Res.* 96, 20337–20351.
- Mueller, R.D., Roest, W.R., Royer, J.-Y., Gahagan, L.M., Sclater, J.G., 1993. A digital age map of the ocean floor. *SIO Reference Series* 93–30. Scripps Institute of Oceanography, La Jolla, CA.
- Nicolas, A., Christensen, N.I., 1987. Formation of anisotropy in upper mantle peridotites: a review. In: Fuchs, K., Froidevaux, C. (Eds.), *Composition, Structure, and Dynamics of Lithosphere–Asthenosphere System*. Geodyn. Ser., Vol. 16. American Geophysical Union, Washington, DC, pp. 111–123.
- Nishimura, C.E., Forsyth, D.W., 1989. The anisotropic structure of the upper mantle in the Pacific. *Geophys. J.* 96, 203–229.
- Nolet, G., 1975. Higher Rayleigh modes in western Europe. *Geophys. Res. Lett.* 2, 60–62.
- Nolet, G., Grand, S.P., Kennett, B.L.N., 1994. Seismic heterogeneity in the upper mantle. *J. Geophys. Res.* 99, 23753–23766.
- Plank, T., Langmuir, C.H., 1992. Effects of the melting regime on the composition of the oceanic crust. *J. Geophys. Res.* 97, 19749–19770.
- Pollack, H.N., Chapman, D.S., 1977. On the regional variation of heat loss, geotherms, and lithospheric thickness. *Tectonophysics* 38, 279–296.
- Revenaugh, J.S., Jordan, T.H., 1991a. Mantle layering from ScS reverberations: 1. Waveform inversion of zeroth-order reverberations. *J. Geophys. Res.* 96, 19749–19762.
- Revenaugh, J.S., Jordan, T.H., 1991b. Mantle layering from ScS reverberations: 2. The transition zone. *J. Geophys. Res.* 96, 19763–19780.
- Revenaugh, J.S., Jordan, T.H., 1991c. Mantle layering from ScS reverberations: 3. The upper mantle. *J. Geophys. Res.* 96, 19781–19810.

- Rigden, S.M., Gwanmesia, G.D., Fitzgerald, J.D., Jackson, I., Lieberman, R.C., 1991. Spinel elasticity and the seismic structure of the transition zone of the mantle. *Nature* 345, 143–145.
- Ringwood, A.E., 1975. *Composition and Petrology of the Earth's Mantle*. McGraw-Hill, New York.
- Rutland, R.W.R., 1981. Structural framework of the Australian Precambrian. In: Hunter, D.R. (Ed.), *Precambrian of the Southern Hemisphere*. Elsevier, Amsterdam, pp. 1–32.
- Sato, H., Sacks, I.S., Murase, T., 1989. The use of laboratory velocity data for estimating temperature and partial melt fraction in the low-velocity zone: comparison with heat flow and electrical conductivity studies. *J. Geophys. Res.* 94, 5689–5704.
- Schlue, J.W., Knopoff, L., 1977. Shear wave polarization anisotropy in the Pacific basin. *Geophys. J. R. Astron. Soc.* 49, 145–165.
- Shearer, P.M., 1990. Seismic imaging of upper mantle structure with new evidence for a 520-km discontinuity. *Nature* 344, 121–126.
- Shearer, P.M., 1993. Global mapping of upper mantle reflectors from long-period SS precursors. *Geophys. J. Int.* 115, 878–904.
- Silver, P.G., 1996. Seismic anisotropy beneath the continents: probing the depths of geology. *Annu. Rev. Earth Planet. Sci.* 24, 385–432.
- Silver, P.G., Chan, W.W., 1991. Shear wave splitting and subcontinental mantle deformation. *J. Geophys. Res.* 96, 16429–16454.
- Spence, D.A., Turcotte, D.L., 1990. Buoyancy-driven magma fracture: a mechanism for ascent through the lithosphere and the emplacement of diamonds. *J. Geophys. Res.* 95, 5133–5139.
- Su, W.-J., Woodward, R.L., Dziewonski, A.M., 1994. Degree 12 model of shear velocity heterogeneity in the mantle. *J. Geophys. Res.* 99, 6945–6980.
- Thompson, A.B., 1992. Water in the Earth's upper mantle. *Nature* 358, 295–302.
- Tong, C., Gudmundsson, O., Kennett, B.L.N., 1994. Shear waves splitting in refracted waves returned from the upper mantle transition zone beneath northern Australia. *J. Geophys. Res.* 99, 15783–15799.
- van der Hilst, R.D., Engdahl, R., Spakman, W., Nolet, G., 1991. Tomographic imaging of subducted lithosphere below north-west Pacific island arcs. *Nature* 353, 37–43.
- Vidale, J.E., Benz, H.M., 1992. Upper mantle seismic discontinuities and the thermal structure of subduction zones. *Nature* 356, 678–683.
- Vinnik, L.P., Makeyeva, L.I., Milev, A., Usenko, A.Y., 1992. Global patterns of azimuthal anisotropy and deformations in the continental mantle. *Geophys. J. Int.* 111, 433–447.
- Vinnik, L.P., Green, R.W.E., Nicolaysen, L.O., 1995. Recent deformations of the deep continental root beneath southern Africa. *Nature* 375, 50–52.
- Vinnik, L.P., Chevrot, S., Montagner, J.-P., 1997. Evidence for a stagnant plume in the transition zone?. *Geophys. Res. Lett.* 24, 1007–1010.
- Walck, M., 1984. The P wave upper mantle structure beneath an active spreading center: the Gulf of California. *Geophys. J. R. Astron. Soc.* 76, 697–723.
- Weidner, D.J., Wang, Y., 1998. Chemical and clapyron induced buoyancy at the 660-km discontinuity. *J. Geophys. Res.* 103, 7431–7442.
- Wessel, P., Smith, W.H.F., 1995. New version of generic mapping tools released. *Eos* 76, 329.
- Woodhouse, J.H., Dziewonski, A.M., 1984. Mapping the upper mantle: three-dimensional modeling of Earth structure by inversion of seismic waveforms. *J. Geophys. Res.* 89, 5953–5986.
- Zhang, Z., Lay, T., 1993. Investigation of upper mantle discontinuities near northwestern Pacific subduction zones using precursors to sSH. *J. Geophys. Res.* 98, 4389–4406.
- Zhang, Y.-S., Tanimoto, T., 1993. High-resolution global upper mantle structure and plate tectonics. *J. Geophys. Res.* 98, 9793–9823.
- Zhao, L., Jordan, T.H., 1998. Sensitivity of frequency-dependent travel times to laterally heterogeneous, anisotropic Earth structure. *Geophys. J. Int.* 133, 683–704.